Molecular Dynamics of Spin Crossover: the (P,T) phase diagram of [Fe(PM-BIA)2(NCS)2]

Alain Marbeuf, Samir F. Matar, Philippe Négrier, Lara Kabalan, Jean-François Létard, Philippe Guionneau

Molecular dynamics of spin crossover: The (P,T) phase diagram of $[Fe(PM\text{-}BIA)_2(NCS)_2]$

A. Marbeuf [a], S.F. Matar [b,c,*], P. Négrier [a], L. Kabalan [b,c], J.F. Létard [b,c], P. Guionneau [b,c]

[a] Université de Bordeaux-CNRS, LOMA, 351 cours de la Libération, F-33400 Talence, France
[b] CNRS, ICMCB, UPR 9048, F-33600 Pessac, France
[c] Univ. Bordeaux, ICMCB, UPR 9048, F-33600 Pessac, France

Keywords:
Spin-crossover complex
DFT
Molecular dynamics
(P,T) phase diagram

A B S T R A C T

The spin crossover properties and the domains of existence of the different phases for the [Fe(PM BIA)$_2$(NCS)$_2$] complex are obtained from combining DFT and classical molecular dynamics (MD). The potential energy surfaces expressed in the Morse form for Fe N interactions are deduced from molecular DFT calculations and they allow producing Infra Red and Raman frequencies. These Fe N potentials inserted in a classical force field lead from MD calculations to the relative energies of the high spin and low spin configurations of the orthorhombic structure. The MD investigations have also allowed assessing the experimental (P,T) phase diagram by showing the monoclinic polymorph in its two spin states, and generating two triple points.

1. Introduction

Few inorganic transition metal ion complexes exhibit two electronic states of their *d* electrons, the Low Spin state (*LS*) and High Spin state (*HS*). The switching between these two states is subjected to small energy magnitudes and the transitions can be achieved with external constraints such as temperature and pressure as well as by applying light. The observed behavior, referred to as Spin CrossOver (*SCO*) and mainly studied in Fe^{II} complexes, has been widely investigated by research groups worldwide both from the fundamental and applied (display applications,...) [1–4]. The transition temperature at which there is same proportion of *LS* and *HS* is called $T_{1/2}$. In the case of first order transition, the thermal hysteresis is described by $T_{1/2}\uparrow$ and $T_{1/2}\downarrow$ associated with the corresponding enthalpy change ΔH. One of these complexes, $[Fe(PM\ BIA)_2(NCS)_2]$,[1] is characterized by iron surrounded by a distorded octahedron involving two *N* (2′ pyridylmethylene) (PM) and two 4 aminobiphenyl (BIA) ligands and completed by two thiocyanate anions. It is known to undergo a gradual *SCO* at $T_{1/2} = 190$ K in the monoclinic polymorph (II phase, $Z = 4$, space group $P2_1/c$) [1–8]. A very abrupt transition is observed for the orthorhombic polymorph (I phase, $Z = 4$, space group *Pccn*) with $T_{1/2}\uparrow = 173$ K and $T_{1/2}\downarrow = 168$ K between the low spin (*LS*, S = 0) to the high spin state (*HS*, S = 2) of the Fe^{2+} ion [4]. Among its interesting magneto optical properties, this *SCO* may be light induced, the limit temperature above which a photomagnetic effect in a material is erased the so called T_{LIESST} (for « *Light Induced Excited Spin State Trapping* ») depending strongly on the structural distortion of the $3d^6$ Fe^{2+} environment [9] and/or the nature of the ligand [10]. As often [8,11,12], pressure plays a role in the opposite sense of temperature in as far the starting spin state is the high spin: by increasing pressure, both I and II polymorphs of FePMBIA yield a *HS* → *LS* transition [13].

In such a complex compound, density functional theory (*DFT*) [14,15] approach is useful for understanding the property differences between the two spin states, namely ionic charges of the Fe^{2+} cation or the N atoms, geometric molecular building and magnetic properties, as shown in the study of Fe^{II} complexes: the *SCO* with a measurable $T_{1/2}$ originates from the crystal field around Fe^{II} which must be of medium strength such with use of *N* based ligands [16]. But *ab initio* methods cannot well explain intermolecular interactions in molecular crystals, because dispersion forces are insufficiently reproduced. Consequently, the obtained energy values may be far from experiments, leading sometimes to wrong hierarchy stability between the spin states. In view of this drawback the determination of the transition enthalpy $\Delta H_{LS\rightarrow HS}$ is made difficult.

For that, classical methods, such as molecular dynamics (*MD*), where van der Waals forces or hydrogen bonding may be modeled inside a generalized atom atom force field, are preferred. Nevertheless, the knowledge of atomic charges (q_i) and of the potential energy surface (*PES*) deduced from molecular *DFT* calculations, is very often used as a starting step in a *MD* approach, as in [17]; the quantum results allow evaluating force field parameters. In

* Corresponding author at: CNRS, ICMCB, UPR 9048, F-33600 Pessac, France.
E-mail address: matar@icmcb-bordeaux.cnrs.fr (S.F. Matar).

[1] $[Fe(PM\text{-}BIA)_2(NCS)_2]$ complex will be called thereafter as FePMBIA.

this context we may define such an original methodology, combin ing *DFT* calculations and molecular dynamics, first in the molecular state and finally in the crystalline one, as "semi classical molecular dynamics".

2. Methodology

Because the classical intramolecular force field comprises elec trostatic forces acting between atomic charges, stretching 2 body interactions, bending 3 body forces and dihedral 4 body interac tions, in order to model a molecule, the first step is a *DFT* proce dure. *Ab initio* calculations applying the *GAUSSIAN* code to the FePMBIA molecule in its two spin states are firstly carried out, fol lowed by a Mulliken analysis [18]. For this purpose, the hybrid *B3LYP** functional, with effective core potential *LANL2DZ* (*Los Alamos National Laboratory with Double Zeta* polarization) function, has been used for all atoms. For a reminder, in the original formu lation of the *B3LYP* hybrid functional, one modification of the ex change weighting parameter called *B3LYP** was proposed by Reiher [19]. Resulting optimized molecular structure and point charges allow generating the *PES*. The curve is fitted with Morse V_{Fe-N} and harmonic V_{Fe-C-N} potentials, by varying alternatively one of the three Fe N_i distances of FePMBIA in each spin state while the two others remain constant. Only I phase whose vibra tion properties are experimentally known has been used.

In a second step, *MD* simulations are performed including other intramolecular interactions described by 2 body, 3 body and 4 body potentials at the level of the molecule. Internal van der Waals interactions occurring between pyridine and phenyl rings or describing S...H hydrogen bonds must be added. All these param eters are adjusted with respect to the molecular geometry and the spectroscopic properties by using the *DL POLY* code [20] which yields a molecular field for each spin state.

Then these generalized force fields can be applied to the molec ular crystal lattice. After a minimization step at 1 K for both spin states, *MD* simulations are performed up to 300 K by increasing temperature. Similar *MD* runs are done by cooling. Best van der Waals parameters are searched for, in order to reproduce struc tures both in *LS* state (25 K and 140 K) and *HS* state (298 K) [2,4,21].

With these final intermolecular force fields, the complete set of runs allow evaluating respectively $T_{1/2}\uparrow$ and $T_{1/2}\downarrow$ and transition enthalpy $\Delta H_{LS\to HS}$ at $T_{1/2}$, the so called $\Delta H_{1/2}$. $T_{1/2}$ and $\Delta H_{1/2}$ are re lated, as shown in a phenomological thermodynamical view, by modeling the *LS HS* domain mixture as a regular solid solution [22]. In such a way, the Gibbs free energy $G_{LS\to HS}$, referred to the *LS* state, is expressed as a function of the molar fraction of *HS* state γ_{HS} in the crystal according to:

$$G_{LS\to HS} \quad \gamma_{HS}\Delta H_{LS\to HS} + \Omega\gamma_{HS}(1 \quad \gamma_{HS}) + RT\{[\gamma_{HS}\ln\gamma_{HS} + (1 \quad \gamma_{HS})\ln(1 \quad \gamma_{HS})] \quad \Delta S_{LS\to HS}\} \qquad (1a)$$

Ω is a constant, which may be related to the interacting energy between domains and the domain size [23]. $\Delta S_{LS\to HS}$ represents the transition entropy during the spin transition, and R the ideal gas constant. Searching the equilibrium condition in the crystal as:

$$\partial G_{LS\to HS}/\partial\gamma_{HS} \quad 0, \qquad (1b)$$

a relationship is found in this model giving temperature as a func tion of thermodynamical functions:

$$T \quad [\Delta H_{LS\to HS} + \Omega(1 \quad 2\gamma_{HS})]/\{R\ln[(1 \quad \gamma_{HS})/\gamma_{HS}] + \Delta S_{LS\to HS}\}, \qquad (1c)$$

At the so called $T_{1/2}$ temperature for which $\gamma_{HS} = 1/2$, Eq. (1c) implies that $T_{1/2}$ is Ω independent, as for an ideal mixture, and $T_{1/2} \quad \Delta H_{LS\to HS}/\Delta S_{LS\to HS}$. For other temperatures, $\gamma_{HS} \neq 1/2$, even if $\Omega = 0$; the enthalpy function will be evaluated by using Eq. (1c) and assuming a Boltzman distribution of the *HS* domains. The var iation enthalpy is then deduced as the enthalpic term of the Gibbs free energy:

$$\Delta H \quad \gamma_{HS}\Delta H_{LS\to HS} + \Omega\gamma_{HS}(1 \quad \gamma_{HS}) \qquad (1d)$$

with an S shape, more pronounced when $\Omega \geqslant 2RT_{1/2}$.

At the same time, cell parameter variations versus temperature may be directly compared to experiments [3]. Isotherm and isobar *MD* runs are also performed on the *LS* state (I phase) in order to study its instability, the resulting I → II transition in both spin states and to assess the experimental (P,T) phase diagram [13,24].

3. Force field in the two spin states of a FePMBIA molecule

3.1. Potential energy surface fit

Fig.1 gives a molecular view of the FePMBIA complex. The num bering of the nitrogen atoms is the following: N_1 is attached to the pyridylmethylene group (PM), N_2 to the aminobiphenyl ring (BIA) and N_3 belongs to thiocyanate anion. *DFT* calculations are achieved for each spin state by a geometry optimization of this structure. The *PES* fit requires studying successively its sections by two of the Fe N_1, Fe N_2 and Fe N_3 distances, in order to know its varia tion with Fe N_1, Fe N_2 and Fe N_3 distances. Except the last case, the molecular geometry constraints imply that, when dFe N_1 dis tances vary, θFe N_2 C angles are not constant. In the same man ner, θFe N_1 C angles vary with dFe N_2. Point Mulliken charges deduced from *DFT* calculations are given in Table 1. For Fe^{2+}, they show that $q_{LS} \approx 3/2\ q_{HS}$. Thus, it will not be surprising that exis tence of point Mulliken charges devoted to one spin state will im ply two different intramolecular force fields.

All Fe N_i ($i = 1,\ldots,3$) 2 body interactions are described by a Morse expression:

$$V_{Morse}(r_{ij}) \quad E^o_{ij}\left[\left\{1 \quad \exp(\ \rho_{ij}(r_{ij} \quad r^o_{ij}))\right\}^2 \quad 1\right] \qquad (2)$$

where E^o_{ij} is the potential depth, ρ_{ij} the electronic hardness and r^o_{ij} the equilibrium distance between two i and j species. It needs to be mentioned here that for the commodity of the many parameters for the six fits, we chose to make constant the ρ_{ij} value to 1.33 Å ^{1} independently from the nature of N_i and of the spin state. A con stant value of ρ_{ij} is currently used in classical force field, even if the coordination polyhedra around a specific atom i are of different types and strongly distorted (see as an example, [25]).

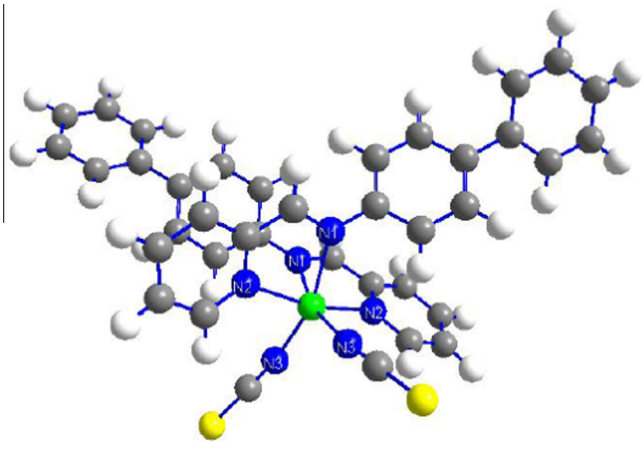

Fig. 1. Molecular view of the $Fe(PM\text{-}BIA)_2NCS_2$ complex. The numbering of the nitrogen atoms is the one found within the text, figures and tables.

Table 1
Mulliken charges of atoms in the Fe–$(N)_6$ octahedron (in e).

	LS	HS
Fe	1.5099	1.0442
N_1	−0.7245	−0.7662
N_2	−0.7678	−0.6936
N_3	−0.7567	−0.7326

Furthermore we used harmonic 3 body interactions for the Fe N_1 C and Fe N_2 C angles:

$$V_{harm}(\theta_{ijk}) \quad 1/2k_{ijk}(\theta_{ijk} \quad \theta^{\circ}{}_{ijk})^2 \tag{3}$$

where k_{ijk} is the stiffness constant of the angle θ_{ijk} and θ^{o}_{ijk} the equi librium angle.

Taking into account the Coulomb forces due to $q_{Fe^{2+}}$ and q_{N^i} charges, Fig. 2(a) (c) show the Morse fit of *PES* combined with angular harmonic potential (case of N_1 and N_2) when Fe^{2+} is in the *LS* state. Fig. 3(a) (c) give the same kind of results for the *HS* state. All the corresponding parameters are given in Table 2. It can be noted that the minimum position r_{min} is smaller than r^{o}_{ij} as a consequence of the influence of the Coulomb field leading to a slightly modified curvature of the total potential $V(r_{ij}) = V_{Morse}(r_{ij}) + V_{Coulomb}(r_{ij})$ as seen by the 2nd order derivative:

$$[d^2V(r_{ij})/dr^2_{ij}]_{\min} \quad 2E^{o}_{ij}\rho^2_{ij}\exp[\ \ 2\rho_{ij}(r_{\min} \quad r^{o}_{ij})] + 2kq_iq_j \times (1 \quad 0.5 \times \rho_{ij}r_{\min})/r^3_{\min} \tag{4}$$

where k is the Coulomb constant. From Table 2, the potential depths in the *LS* state ($E^{o,LS}_{FeN_1}$, $E^{o,LS}_{FeN_2}$, $E^{o,LS}_{FeN_3}$) are deeper than in the *HS* state ($E^{o,LS}_{FeN_1}$, $E^{o,LS}_{FeN_2}$, $E^{o,LS}_{FeN_3}$) and:

$E^{o,LS}_{FeN_1} \sim 3E^{o,HS}_{FeN_1}$ and $E^{o,LS}_{FeN_2} \sim 3E^{o,HS}_{FeN_2}$.

3.2. Intramolecular force field

The force field devoted to a given spin state requires the input of:

(i) all 2 body stretching harmonic interactions, such as C H, C C, C N, C S, N S, but also weak N N octahedron interactions;
(ii) 3 body interactions, namely H C C, H C N, C C C, C C N, which will be described by bending harmonic potentials associated (Eq. (3)) and coupled potentials. There are two extra contributions needing to be accounted for in the cou pling potentials; these are the coupling between adjacent bonds for species i, j and i, k in $V(r_{ij},r_{ik})$:

$$V(r_{ij}, r_{kj}) \quad A_{ijk}(r_{ij} \quad r^{\circ}{}_{ij})(r_{ik} \quad r^{\circ}{}_{ik}) \tag{5}$$

and the potential accounting for the bond and the angle $V(r_{ij}, \theta_{ijk})$:

$$V(r_{ij}, \theta_{jk}) \quad A_{ijk}(r_{ij} \quad r^{\circ}{}_{ij})(\theta_{ijk} \quad \theta^{\circ}{}_{ijk}) \tag{6}$$

in both Eqs. (5), (6) A_{ijk} is a stiffness constant.

(iii) 4 body dihedral and inversion interactions for maintaining the planarity of pyridine and of phenyl rings as well as for describing low vibration modes. The 4 body dihedral poten tial is:

$$V_{cos} \quad A_{ijkl}[1 + \cos(m\phi_{ijkl} \quad \delta_{ijkl})] \tag{7}$$

where A_{ijkl} is a stiffness constant, ϕ_{ijkl} is the dihedral angle and δ_{ijkl} the reference dihedral angle acting as an out of phase. Interactions due to inversion (with the ϕ_{ijkl} angle) correspond to the following expression:

$$V_{plan} \quad A_{ijkl}[1 \quad \cos(\phi_{ijkl})] \tag{8}$$

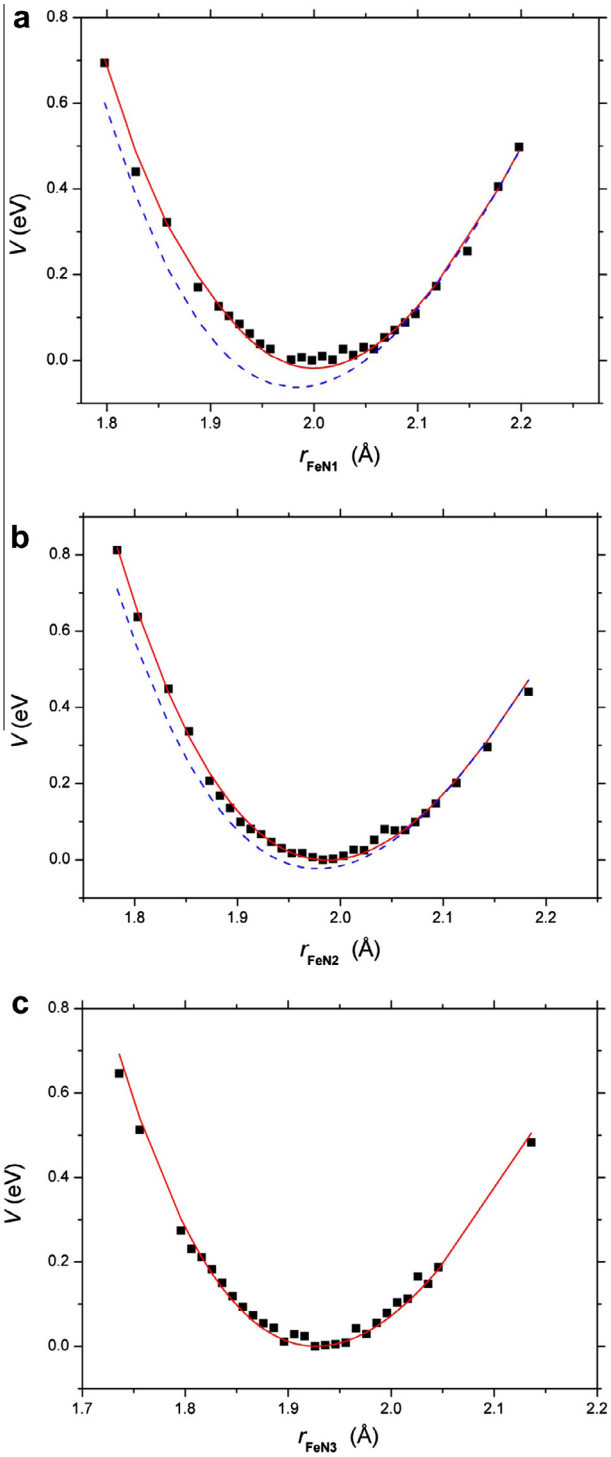

Fig. 2. Fit of the quantum potential energy surface (*PES*) in the *LS* spin state by combining Fe–N_1 Morse and Coulomb potentials with (straight red line in a) or without N_2–Fe–C harmonic potential (dotted blue line); by combining Fe–N_2 Morse and Coulomb potentials with (straight red line in b) or without N_1–Fe–C harmonic potential (dotted blue line); by using Fe–N_3 Morse and Coulomb potentials (straight red line in c). Black squares symbolize the *PES* values.

Starting values for parameters involved in all these intramolecular potentials, i.e. Eqs. (2), (3), (5) (8), come from the *COMPASS* force field which is devoted to organic molecules [26].

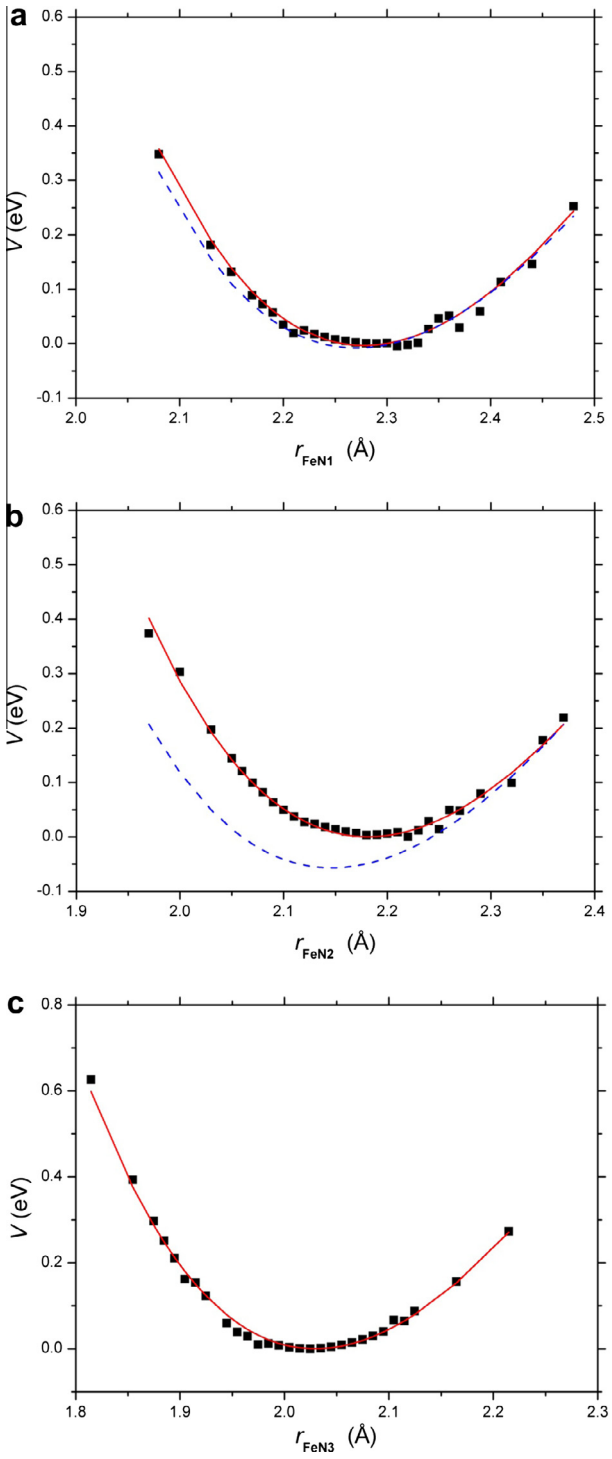

Fig. 3. Fit of the quantum potential energy surface (*PES*) in the *HS* spin state. Symbols have the same meaning as in Fig.2.

(iv) long range potentials in a Lennard Jones form $V_{LJ}(r_{ij})$ have to be accounted for to describe the van der Waals interactions between adjacent phenyl rings and S...H hydrogen bonds and to reproduce the deformation modes involving two ligands connected to Fe^{2+}:

$$V_{LJ}(r_{ij}) \quad 4\varepsilon_{ij}^{o}[(\sigma_{ij}/r_{ij})^{12} \quad (\sigma_{ij}/r_{ij})^{6}] \qquad (9)$$

ε_{ij}^{o} is the potential depth, σ_{ij} the distance at which the long range i j interaction vanishes. The corresponding parameter values are extracted from [27].

The r_{ij}^{o} equilibrium Morse values are changed in order to match the *MD* geometry (r_{min}) with experiment. In the same way the stiffness constants in the other 2 body potentials and in the 3 body potentials, as well as in the coupled ones, are modified according to the vibration modes. For both spin states, the complete force fields are given as Supplementary informations (Tables S1 and S2).

3.3. Application to the molecule in LS and HS spins states

The established force fields are applied to the FePMBIA molecule in *MD* runs by using *DL POLY* code. All simulations are performed at 0 K in the *NVT* ensemble coupled to a Berendsen thermostat (relaxation time constant = 0.1 ps) [28], with a long range distance cut off equal to 12 Å when calculating Coulomb forces by the Ewald method [29] or van der Waals interactions. As a result, Table 3 provides a comparison between experimental and *MD* octahedral FeN_6 geometries for the two spin states. The d_{Fe-N} distance magnitudes are well reproduced together with the θ_{N-Fe-N} angles. The expected trend for a greater distortion in *HS* octahedron versus *LS* is found as exhibited by distance and angle extrema:

Δd_{HS} 0.21 $> \Delta d_{LS}$ 0.03 Å; $\Delta\theta_{HS}$ 26.4 $> \Delta\theta_{LS}$ 13.7 deg

Low frequency vibration modes are well reproduced. Table 4 shows that the difference $\Delta\nu_{MD}$ between measurements of Hoeffer [30] and *MD* results does not exceed 23 cm^{-1} for octahedral Fe N stretching modes, whereas *DFT* agreement is better ($\Delta\nu_{DFT} < 12$ cm^{-1}). The position of the bending modes of the N C S group appear below experimental values ($\Delta\nu_{MD} < 35$ cm^{-1} in *LS* state, <10 cm^{-1} in *HS* state); agreement is better for stretching C S and C N modes in both states ($\Delta\nu_{MD} < 24$ cm^{-1}). In the high frequency region due to the C H modes, well matching values are found upon comparing with *DFT* calculations; for these modes, $0 < \nu_{LS}$ $\nu_{HS} < 49$ cm^{-1}, smaller than with *DFT* values (Table S3 as supplementary informations).

For each spin state, the total energy found at 0 K (E_{LS} = 26.11 eV, E_{HS} = 25.99 eV) yields directly the molecular total energy difference between the two spin states $\Delta E_{LS\to HS}$:

$$\Delta H_{LS\to HS} \quad \Delta E_{LS\to HS} + P\Delta V_{LS\to HS} \qquad (10)$$

Because MD runs of a single molecule are only done under the *NVT* ensemble in the *DL POLY* code [20], $\Delta V_{LS\to HS} = 0$ in this expression, and therefore, $\Delta E_{LS\to HS}$ gives directly the transition enthalpy: $\Delta H_{LS\to HS} = 0.12$ eV = 11.2 kJ/mol. Incidentally, this value is close to the experimental one determined by differential scanning analysis (*DSC*) on FePMBIA crystalline powders, obtained under atmospheric pressure (*NPT* conditions): (i) in the 160 190 K range, by [2] $\Delta H_{LS\to HS} = 10.06$ kJ/mol; (ii) more recently by [31] $\Delta H_{LS\to HS} = 11.5$ kJ/mol. Consequently, rigourously speaking, these two obtained values cannot be compared and another simulation method will be preferred calling for the whole crystal system which is modeled in the *NPT* ensemble as detailed in the following.

4. I-FePMBIA crystal in the two spin states

4.1. Intermolecular field in the crystal phase

At this step, molecular force field in one of the two spin states may be applied in *MD* runs to the crystal. For this purpose, the experimental structure corresponding with its three cell parameters (a, b and c), determined at 25 K and at room temperature, is used as a starting configuration and repeated in each crystallographic direction. The resulting 8 cell « box » is optimized at 0 K

Table 2
Parameters for Morse potentials describing the 2-body Fe–N_i interactions and harmonic potentials of 3-body Fe–N_i–C interactions deduced from the *DFT* potential energy surface.

	E^o (eV)	ρ (Å ^{1})	r^o (Å)	$r_{min}^{(opt)}$ (Å)	$r_{min}^{(DFT)}$ (Å)	k (meV/deg^2)	$\theta_{min}^{(opt)}$ (deg)	$\theta_{min}^{(DFT)}$ (deg)
LS								
Fe–N_1	1.54(1)	1.33	2.34(1)	2.000(5)	1.998	1.0	119(1)	114.5
Fe–N_2	1.33(1)	1.33	2.38(1)	1.990(5)	1.983	0.52	119(1)	114.3
Fe–N_3	1.23(2)	1.33	2.355(5)	1.925(5)	1.936			
HS								
Fe–N_1	0.44(2)	1.33	2.78(1)	2.280(5)	2.28	0.52	119(1)	117.0
Fe–N_2	0.405(5)	1.33	2.68(1)	2.180(5)	2.170	0.92	119(1)	113.5
Fe–N_3	0.92(2)	1.33	2.41(2)	2.03(1)	2.014			

Table 3
Octahedral geometry of the Fe^{2+} environment: comparison between experiments and molecular dynamics.

Distances (Å)	LS			HS		
	r^o	exp[a]	MD	r^o	exp[b]	MD
Fe–N_1	2.105	1.965	1.967	2.586	2.251	2.250
Fe–N_2	2.100	1.964	1.967	2.640	2.230	2.229
Fe–N_3	2.067	1.938	1.934	2.288	2.040	2.041
N_1–N_1		2.695	2.695		2.850	2.850
N_1–N_2		2.546	2.552		2.707	2.707
“		2.896	2.893		3.246	3.246
N_1–N_3		2.831	2.828		3.191	3.191
N_2–N_3		2.837	2.844		3.030	3.030
“		2.781	2.780		3.293	3.293
N_3–N_3		2.695	2.694		2.969	2.970
Angles (deg)						
N_1–Fe–N_1		86.58	86.47		78.58	78.60
N_1–Fe–N_2		80.79	80.86		74.37	74.40
“		94.98	94.61		92.90	92.93
N_1–Fe–N_3		92.98	92.90		95.97	95.96
N_2–Fe–N_3		90.88	90.89		90.33	90.30
“		93.27	93.54		100.86	100.84
N_3–Fe–N_3		88.08	88.29		93.36	93.35

[a] [21].
[b] [2].

in the *NVT* ensemble coupled to a Berendsen thermostat (relaxation time constant = 0.1 ps) with the same cut off as in Section 3.3 (12 Å). Then, isotherm simulations are made in the isostress $N\sigma T$ ensemble coupled to a Berendsen barostat (relaxation time constant = 1.0 ps): (i) to ensure that the average system pressure is maintained to the atmospheric one; (ii) to allow b/a and c/a ratios to vary; (iii) to ensure that the orthorhombic symmetry is conserved (the angles α, β and γ of the simulated cell ought to be very close to 90°). Contrary to an isobar simulation run performed in the *NPT* ensemble, isostress $N\sigma T$ ensemble implies that pressure does not rigorously conserve the angles within the cell. Each run is followed by a new simulation in the isobar *NPT* ensemble with the same relaxation time constants as in the *NVT* or $N\sigma T$ runs.

Table 5
Intermolecular interactions in the two spin states (For “chemical” clarity,the weak potential depths are given in kJ/mol units instead of eV).

	ε_{ij}^o (kJ/mol)	LS	HS
		σ_{ij} (Å)	σ_{ij} (Å)
C…C	0.393	3.040	3.420
C…N	0.357	3.043	3.570
C…S	0.752	3.040	3.741
C…H	0.208	2.900	2.900
N…N	0.324	3.220	3.662
N…S	0.685	3.400	3.846
N…H	0.208	2.900	2.913
S…S	1.439	4.030	4.030
S…H	0.234	2.470	2.900
H…H	0.038	2.150	2.150

It is clear that cell volume and structure will be sensitive to the most numerous van der Waals interactions, that is C…C, C…H and H…H interactions, but also to the more energetic hydrogen bonds (N…H and S…H). Without compressibility data, it is impossible to adjust all the corresponding Lenard Jones potentials (Eq. (9)). Therefore, we introduce the constraint that each potential depth ε_{ij}^o does not depend on the spin state and we modify C…C, C…N, C…S, N…N, N…S, N…H and S…H parameters by looking for their influence on the crystal data at 25 K (*LS* state) and 298 K (*HS* state) and on the corresponding van der Waals contacts. Table 5 gives the complete set of parameters (ε_{ij}^o and σ_{ij}) for both spin states. Between the *LS* and *HS* states, some differences may be noted, mainly for C…S and S…H interactions where respectively $^{LS}\sigma_{S\ H}$ = 3.040 Å is smaller than $^{HS}\sigma_{S\ H}$ = 3.741 Å and $^{LS}\sigma_{S\ H}$ = 2.470 Å smaller than $^{HS}\sigma_{C\ S}$ = 2.900 Å: this means that S…H hydrogen bonds are stronger in the *LS* phase than in the *HS* phase, in agreement with the evolution of corresponding intermolecular distances with T ($^{LS}d_{C\ldots S}$ = 3.796 Å, $^{HS}d_{C\ldots S}$ = 3.901 Å, and $^{LS}d_{S\ H}$ = 2.94 Å, $^{HS}d_{S\ H}$ = 3.03 Å), given by [4,32]. The van der Waals part of the energy E_{vdw} represents a little more of the 1/10 of the total energy ($^{LS}E_{VDW}$ = 281.25 kJ/mol, $^{HS}E_{VDW}$ = 278.90 kJ/mol); but if these intermolecular terms are disregarded, $\Delta H_{LS\rightarrow HS}$ will be underestimated of ∼2.3 kJ/mol.

Table 4
Fe–N and *NCS* group frequencies (in cm ^{1}): comparison between experiments of Hoeffer [30], molecular dynamics and *DFT*.

	LS				HS			
	exp	*MD*	DFT		exp	*MD*	DFT	
			I.R.	Raman			I.R.	Raman
Fe–N	237	250		243	151	128		163
	342	346	339		207	197		208
	364	369	363		246, 259, 271	225	241, 257, 271	
	368		369		326	327, 334		323
δ(N–C–S)	447, 453, 458, 473, 487	418, 431, 446, 452		427, 435, 441	438, 469, 478	429, 460, 488		436, 442, 448
C–S	809, 831, 847	825, 845		770, 775	840	837, 846		779, 783
C–N	2124	2148, 2161		2098, 2109	2074, 2081		2093, 2111	2044, 2067

4.2. Intermolecular interactions in the crystal state: towards thermoinduced transition LS → HS

After this van der Waals interaction determination, we are able to simulate an orthorhombic phase cell in its two spin states at 0 K under atmospheric pressure: the total *HS* energy (E_{HS} = 28.65 eV = 2674.0 kJ/mol) is found to be slightly lower than in the *LS* state (E_{LS} = 28.29 eV = 2640.4 kJ/mol). By constraining the van der Waals potential depths to be independent of the spin state, these total energy values are certainly not correct. Moreover, quantum effects prevail at low temperatures. At these temperatures, because the difference between these values is of the order of their numerical fluctuation (±10 kJ/mol), the transition enthalpy cannot be evaluated precisely through an equation similar to Eq. (10), even if *DL_POLY* code gives us both total energy *E* and enthalpy *H* during each step of a *NPT* or *NσT* run.

A better value for $\Delta^{MD}H_{LS\rightarrow HS}$ must be determined in another manner. For this purpose, the molecular crystal system has to be studied by varying its thermodynamic state through isotherm isobaric runs. Increasing temperature runs are made on *LS* phase at 0 K minimized by applying *LS* field; this field is also used for the resulting room temperature phase but with decreasing temperature, in order to study the hysteresis behavior near the $T_{1/2}$ temperature. Similar approach is used for *HS* phase starting in the 0 298 K temperature range with increasing and decreasing step runs.

As argued in the preceding section, the octahedral geometry and the molecular packing depend strongly of the spin state, yielding a transition of the first kind. During the *LS* *HS* spin state transition, cell parameters and, at least, cell volume will therefore undergo discontinuities, allowing to understand the $T_{1/2}$ transition temperature through crystallographic considerations. Figs. 4(a) (c) give the respective variation of *a*, *b* and *c* cell parameters as a function of *T*. The three curve sets show different behaviors. The *a* curve, obtained when *HS* force field is applied to the *HS* phase, shows the instability of this phase below 100 K, whereas the *c* curves is too imprecise for extracting transition informations. However, the crossing of the *b* curves, obtained with *LS* and *HS* force fields and applied with increasing temperature, specifies more precisely the $T_{1/2}\uparrow$ temperature ($T_{1/2}\uparrow$ = 120 K), which is 50 K lower than the experimental one (173 K, [2]). As a result, the effect of the instability of the *HS* state below 100 K, shown in the evolution of the *a* cell parameter, is found again in the cell volume: by increasing temperature a cell volume expansion occurs at 100 K (Fig. 4(d)). At this temperature, the difference of the cell volume between *LS* and *HS* phases (ΔV_{cell} = 121 Å^3) may be compared to the experimental value deduced form crystal data (ΔV_{cell} = 57.4 Å^3, [3]). The observed relatively large differences in temperature and in volume can be accounted for by the drawbacks of a purely classical model in view of the prevailing quantum effects in this temperature region.

At each run step, the total energy and therefore the enthalpy given by the *DL_POLY* code are spin state dependent. Because of the fluctuations of enthalpy, both for the *LS* configuration with *LS* field on one hand and for the *HS* one with *HS* field on the other hand, the enthalpy difference $\Delta^{MD}H_{LS\rightarrow HS}$ cannot be accurately determined by the corresponding difference. For this purpose, *MD* runs combining increasing and decreasing temperature in the two states will be accurate, because of the possibility to use Eq. (1d). The enthalpy difference $\Delta^{MD}H_{LS\rightarrow HS}$ between the two states is obtained by acting the *LS* field on *LS* and *HS* configurations at increasing temperature, as reported on Fig.5 (lower points): a sharp transition occurs between 140 and 160 K, when γ_{HS} content increases according to Eq. (1a), (1b), (1c), (1d). By using now the *HS* field on both spin state phases during cooling runs (Fig.5, upper points), $\Delta^{MD}H_{LS\rightarrow HS}$ is found not to depart from 14 ± 1 kJ/mol, which corresponds to the absence of *LS* crystal domains (γ_{HS} = 1). Therefore, $\Delta^{MD}H_{1/2}$ may be taken as the value of $\Delta^{MD}H_{LS\rightarrow HS}$, that is $\Delta\Delta^{MD}H_{1/2} \sim 14 \pm 2$ kJ/mol (the slightly lower accuracy is due to the fluctuations of the *LS* background around zero). This *MD* value lies a little above the data arising from *DSC* ($\Delta^{DSC}H_{LS\rightarrow HS}$ = 10.06 kJ/mol, [2]; 11.5 kJ/mol, [31]). A more precise determination of $\Delta^{MD}H_{1/2}$ would be certainly obtained through the evaluation of the Gibbs free energy variation $\Delta^{MD}G_{LS\rightarrow HS}$ resulting from the integration of the hybrid classical Hamiltonian which contains potential and kinetic terms and which describes both *LS* and *HS* spin states (see [20,27]). Nevertheless, the evolution of $\Delta^{MD}H_{LS\rightarrow HS}$ with *T* leads to a transition temperature value ($T_{1/2}$ = 150 K), more precise and higher than the one deduced from the structural results (see above), and therefore in better agreement when compared to the experiments ($T_{1/2}\uparrow$ = 173 K and $T_{1/2}\downarrow$ = 168 K, [2]).

The results of simulations presented here allow also comparisons with experimental structures (25 K, 140 K and 298 K). Then, in the *LS* spin state, Table 6 shows that the *b* parameter is larger by 7.2% at 25 K and 12.5% at 140 K, but this is compensated by a *c* parameter with a lower value (11.7% at 140 K). This is even better shown for the *HS* spin state where the small differences on the three cell parameters compensate perfectly when looking for the V_{cell} cell volume: $\Delta V_{cell}/V_{cell}$ = 0.7%. All this result set leads to prefer the more precise thermodynamical value $T_{1/2}$ = 150 K.

5. Pressure stability of I-FePMBIA crystal: the pressure induced I → II phase transition

The influence of pressure on FePMBIA has been studied by magnetic susceptibility measurements [13], optical reflectivity [8] and completed by a recent neutron diffraction study [24]: the orthorhombic I phase undergoes a transition towards the monoclinic II phase, independently of the spin state. This expectedly means that the (P,T) phase diagram must involve four solid phases LS_I, HS_I, LS_{II} and HS_{II}, and therefore two triple points between three of these four phases. Because it would be difficult to study experimentally these last parts of the (P,T) phase diagram, in particular the respective positions of the triple points, *MD* is helpful for assessing it. Therefore, simulations have been performed in the *NσT* ensemble in different isotherm isobar conditions from 25 to 300 K with pressure up to 20 kbar. All these processes were carried out for orthorhombic [Fe(PM BIA)$_2$(NCS)$_2$] in order to exhibit its instability with increasing pressure. Furthermore, simulating the monoclinic phase in both spin states would have required establishing not only a new intramolecular parameter set, but also to select appropriate van der Waals force field in II phase. It is well admitted to use the same force field for room pressure and high pressure phases, as in B_2O_3 [25]. Because of the symmetry breaking between I and II structures, the corresponding phase transition will be of the first kind and therefore better detected in modeling processes. At low temperature, the cell volumes of I and II in their LS state are known to differ (V_{cell,LS_I} = 3339 Å^3 at 140 K, ($V_{cell,LS_{II}}$ = 3294 Å^3 in metastable state at 120 K, [4]); this means increasing pressure will favor more strongly the $LS_I \rightarrow LS_{II}$ phase transition.

Fig. 6(a) (c) give the respective variations of *a*, *b* and *c* cell parameters as a function of *P* for different isotherms between 25 K and 160 K, when LS_I force field is acting: with increasing *P*, *a* and *c* show a sudden decrease in the range 7 12 kbar for 25 K, 50 K, 80 K, whereas a small *b* jump is observed; a departure of the β angle from 90° increases. Because the resulting volume variation is negative, *SCO* must not occur and therefore, as argued before, a $LS_I \rightarrow LS_{II}$ transition is assumed. For upper isotherms, the *a* and *c* curves have smaller discontinuities, one at lower *P* values, namely around 3 kbar, and the second one at 9 kbar. By comparison with the experiments of [13], two transitions must be taken into account: (i) for the lower transition, by combining *SCO* with

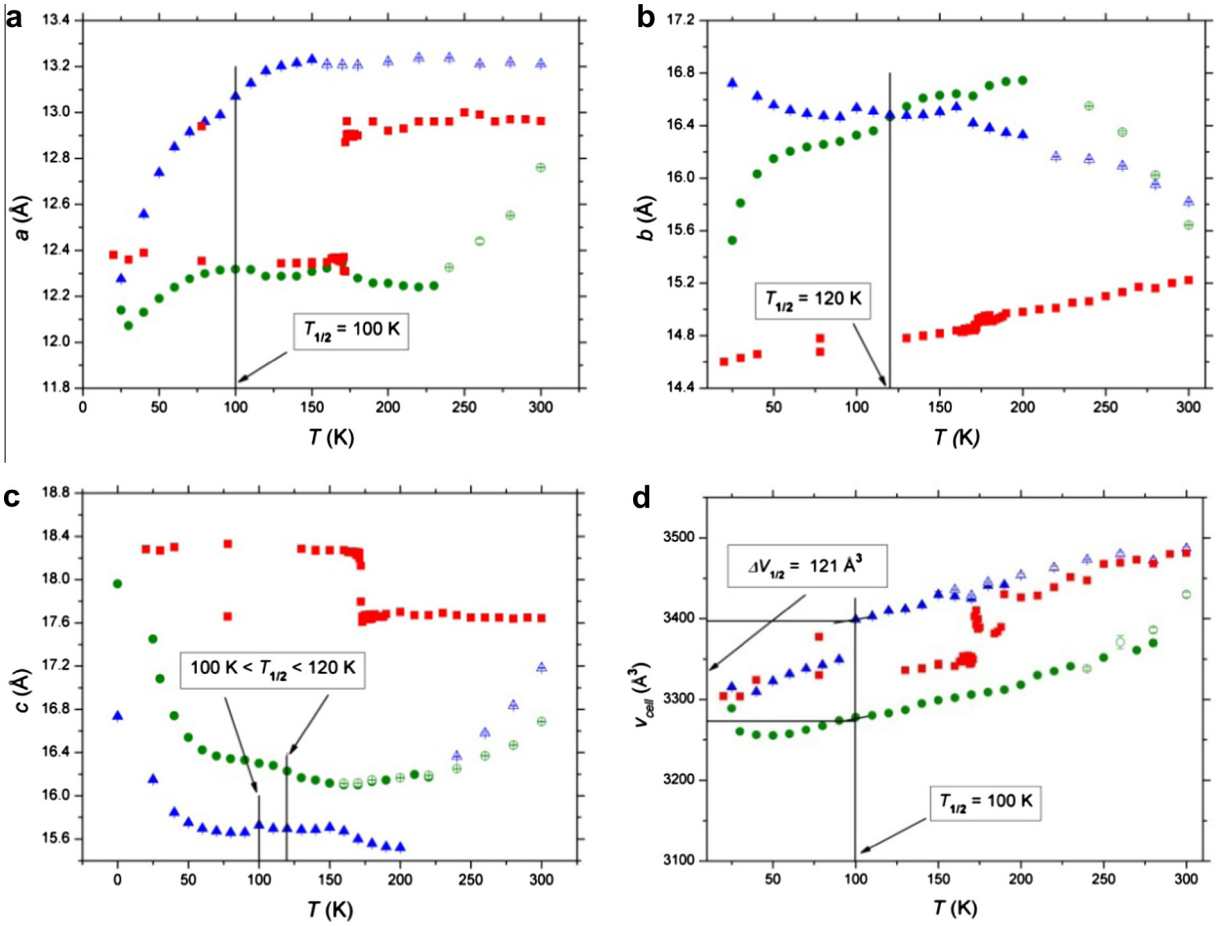

Fig. 4. Evolution of the *a* cell-parameter with temperature in the two spin states and comparison with diffraction data of [3] (a); evolution of the *b* cell-parameter with temperature in the two spin states (b); evolution of the *c* cell-parameter with temperature in the two spin states (c); evolution of the cell volume V_{cell} with temperature in the two spin states (d). Symbol notations are: filled green circles: *LS*-field acting on *LS*-phase at 0 K with increasing temperature; filled blue triangles: *HS*-field acting on *HS*-phase with increasing temperature; empty symbols correspond to runs but in decreasing temperature from 298 K; filled red squares correspond to diffraction data.

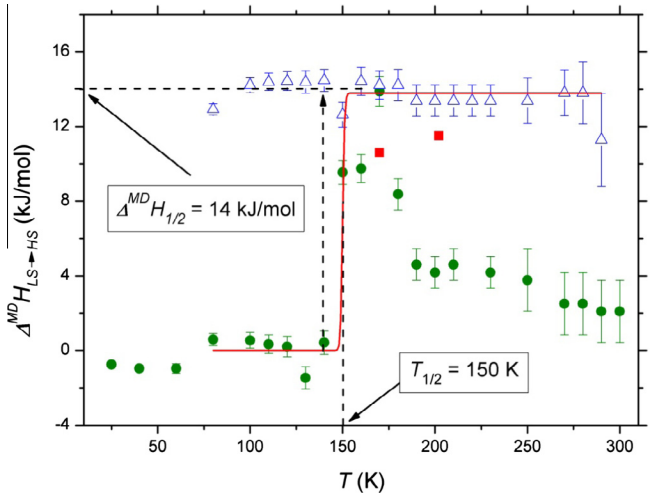

Fig. 5. Evolution of the difference enthalpy between the two spin states versus temperature (heating runs: filled green circles; cooling-down runs: empty blue triangles). Comparison with *DSC* measurements (filled red squares [2,31]).

Table 6
Cell parameters and cell volume in *MD* for the *LS*-state (25 K and 140 K) and for the *HS*-state (140 K and 300 K); comparison with experiments.

	LS			HS		
	MD	exp	diff. (%)	MD	exp	diff. (%)
25 K						
a (Å)	12.1393(4)	12.224(3)[a]	−0.7			
b (Å)	15.5257(6)	14.484(4)[a]	7.2			
c (Å)	17.4516(6)	18.130(5)[a]	−3.7			
V (Å^3)	3289.1(4)	3210(1)[a]	2.5			
140 K						
a (Å)	12.287(1)	12.370(3)[b]	−0.7	13.216(2)		
b (Å)	16.610(2)	14.764(3)[b]	12.5	16.481(2)		
c (Å)	16.146(2)	18.281(4)[b]	−11.7	15.688(2)		
V (Å^3)	3295(1)	3339(2)[b]	−1.3	3417(1)		
298 K						
a (Å)	13.211(3)	12.949(7)[b]	2.0			
b (Å)	15.818(3)	15.183(2)[b]	4.2			
c (Å)	16.688(3)	17.609(5)[b]	−5.2			
V (Å^3)	3487(2)	3462(2)[b]	0.7			

[a] [21].
[b] [2].

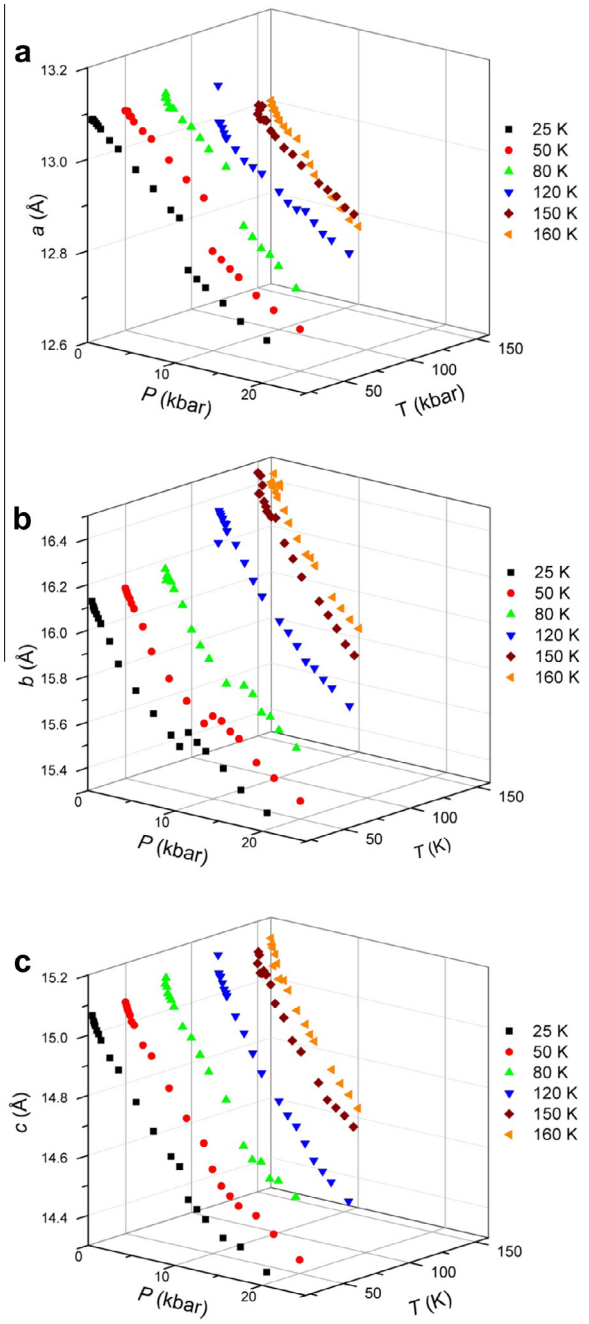

Fig. 6. Evolution of the *a* cell-parameter with increasing pressure between 25 K and 170 K (LS_I-field acting during MD runs) (a); evolution of the *b* cell-parameter (b); evolution of the *c* cell-parameter (c).

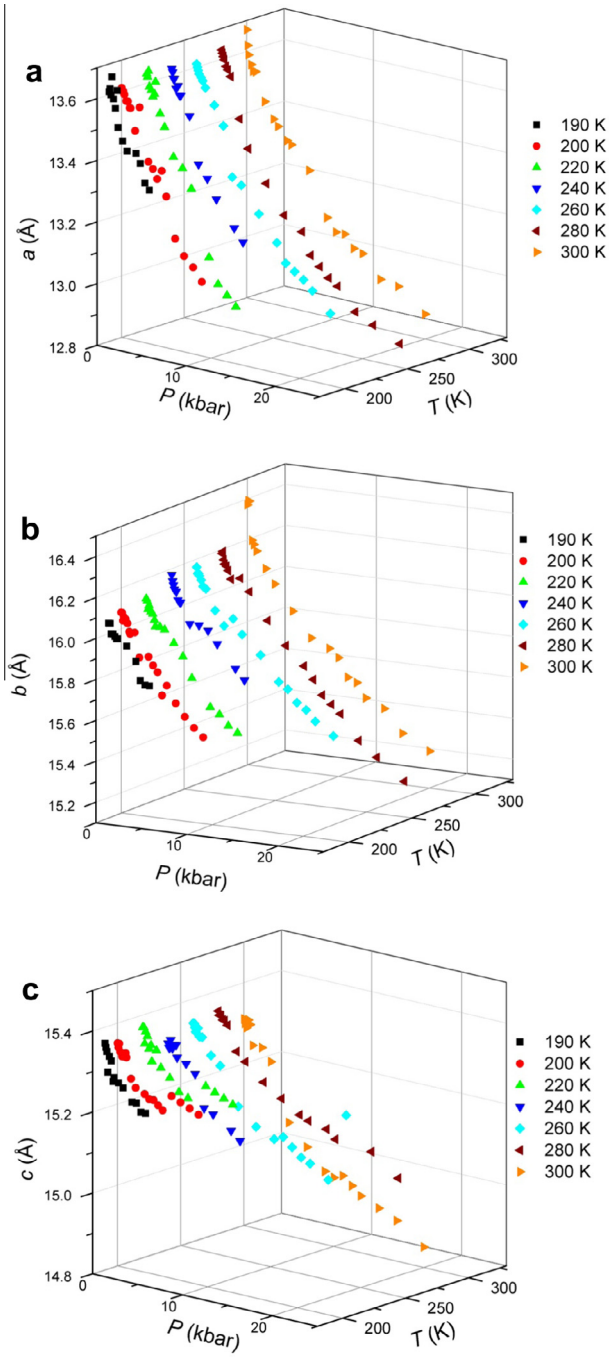

Fig. 7. Evolution of the *a* cell-parameter with increasing pressure between 190 K and 300 K (HS_I-field acting during MD runs) (a); evolution of the *b* cell-parameter (b); evolution of the *c* cell-parameter (c).

a change of symmetry, pressure may authorize a phase in the *HS* state, but more compact than the LS_I polymorph (here ΔV_{cell} = 35 Å^3), leading to a $LS_I \rightarrow HS_{II}$ transition; (ii) because pressure will favor a transition from *HS* to *LS* state, the upper transition will be $HS_{II} \rightarrow LS_{II}$.

When HS_I force field is applied during *MD* runs, HS_I phase will transform logically into a monoclinic HS_{II} polymorph. Fig. 7(a) (c) give the respective variations of *a*, *b* and *c* cell parameters as a function of *P* for different isotherms between 190 K and 300 K: the discontinuities appearing on the *a* and *b* curves, leading to a cell volume contraction, show that the expected $HS_I \rightarrow HS_{II}$ transition occurs at $P \approx 3$ kbar below 280 K, at significantly higher pressure at 300 K ($P \approx 5$ kbar where ΔV_{cell} = 70 Å^3).

Knowing both enthalpy and volume variations during the $LS_I \rightarrow HS_I$ transition at $T_{1/2}$, as given in Section 4.2 ($\Delta H_{1/2}$ = 14.0 kJ/mol, ΔV_{cell} = 121 Å^3), the use of the Clausius Clapeyron relation in its form valid for the transitions of the first kind:

$$(dP/dT)_{T1/2} \quad (\Delta H_{LSI \rightarrow HSI})/(T\Delta V_{LSI \rightarrow HSI}) \qquad (11)$$

allows estimating the slope of the curve corresponding to the $LS_I \rightarrow HS_I$ transition at 1 bar: $(dP/dT)_{T_{1/2}}$ = 0.08 kbar/K. Therefore, Eq. (11) may be used as a guide for the curve delimiting LS_I and HS_I area. One may remark that the value found is 1/2 of the one deduced from the experimental slope of a straight line separating LS_I and HS_I regions built from data of [24] ($(dP/dT)_{T_{1/2}}$ = 0.16 kbar/K).

Nevertheless, this difference is acceptable if we keep in mind the uncertainties found in the evaluation of $\Delta H_{1/2}$, $T_{1/2}$ and ΔV_{cell}. Moreover, the present *MD* value of $(dP/dT)_{T_{1/2}}$ is of the same order to the one found for the [Fe(sal$_2$ trien)][Ni(dmit)$_2$] complex which is known to have its *SCO* near 245 K ($(dP/dT)_{T_{1/2}}$ = 0.06 kbar/K, [11]).

From an experimental point of view, by putting the respective values of $T_{1/2}$ (170 K) and ΔV_{cell} (57.4 Å^3) and knowing the slope dP/dT (0.16 kbar/K), $\Delta H_{1/2}$ can be evaluated from Eq. (11) ($\Delta^{CC}H_{1/2}$ = 23.5 kJ/mol). This value is twice the *DSC* one ($\Delta^{DSC}H_{LS\rightarrow HS}$ = 10.06 kJ/mol [2], 11.5 kJ/mol [31]). In fact, this procedure is certainly incorrect, because in the pressure range involved (1 bar to 6 kbar) the true limiting curve between LS_I and HS_I domains is probably not a straight line, as a consequence of the evolution of the compressibility with pressure in each phase. This means that the slope dP/dT should be smaller than 0.16 kJ/mol, and therefore, the deduced $\Delta^{CC}H_{1/2}$ value closer to the DSC ones.

At this step, the (P,T) phase diagram may be built and compared to experiments (Fig.8). *MD* points are shifted to lower pressure and to lower temperature. Consequently, the calculated triple points are more separated than the ones estimated from experiments: the low pressure triple point which defines the LS_I, HS_I and HS_{II} equilibrium is located at 170 K and a pressure of ~3.0 kbar, the second triple point corresponding to the LS_I, LS_{II} and HS_{II} equilibrium is close to 100 K at ~6.8 kbar. These results may be compared to the experiments [13]. By studying the pressure effect on the hysteresis loop, these authors concluded that the data in the 6 8 kbar range correspond to a *SCO* coupled to a crystallographic phase transition. The present investigation confirms these findings and further provides the nature of the spins states according to the natures of the polymorphs, I and II. In other words, because the data of Ref. [13] take into account the metastability of the LS_I phase in the corresponding thermodynamic conditions which transforms into the HS_{II} phase, the line delimiting HS_I and HS_{II} phase domains in Fig.8 would be located at pressures lower than 7 kbar and at lower temperatures, as found by *MD*.

Another interest in this phase diagram is found by inspecting the slopes of the curves corresponding to the two transitions $LS_I \rightarrow LS_{II}$ and $HS_I \rightarrow HS_{II}$ which are on opposite directions: $(dP/dT)_{LS_I\rightarrow LS_{II}}$ is clearly negative, whereas $(dP/dT)_{HS_I\rightarrow HS_{II}}$ is slightly positive below room temperature. Because pressure favors more compact II phases (LS_{II} or HS_{II}) with a smaller molar volume as shown by [4] ($V_{cell,LS_{II}}$ = 3294 Å^3 < V_{cell,LS_I} = 3399 Å^3), Eq. (11) implies

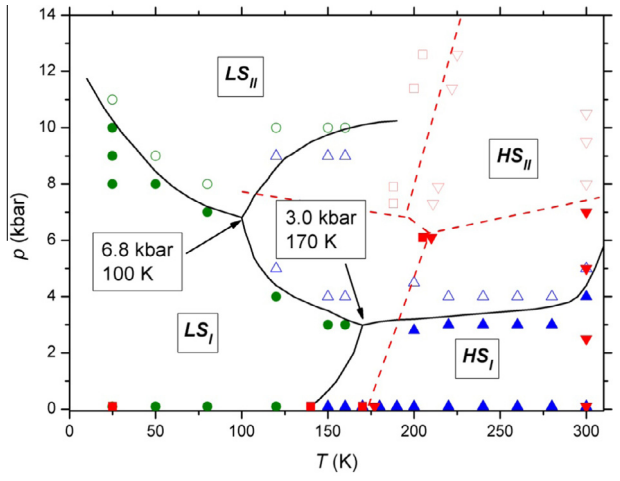

Fig. 8. (P,T) phase diagram showing four solid phases (LS_I: filled green circles; HS_I: filled blue triangles; LS_{II}: empty green circles; HS_{II}: empty blue triangles). Domains delimitated by straight curves generate two triple points. Experimental points from [13,24] are also shown for comparison (LS_I: filled red squares; HS_I: filled red down triangles; LS_{II}: empty red square; HS_{II}: empty red up triangles).

that pressure and temperature play antagonist roles during the $LS_I \rightarrow LS_{II}$ transition with a positive enthalpy variation $\Delta H_{LS_I\rightarrow LS_{II}}$. On the other hand, the $H_{HS_I\rightarrow HS_{II}}$ transition will correspond to a small negative enthalpy variation $\Delta H_{HS_I\rightarrow HS_{II}}$, associated, or not, to a small cell volume variation at room temperature, and to a significant cell volume contraction for *T* below 280 K. This last assumption is confirmed by the behavior of the corresponding experimental cell volumes [4,24,32]: starting from nearly equal values at 293 K ($V_{cell,HS_{II}}$ = 3464 Å^3; (V_{cell,HS_I} = 3462 Å^3), the two volume values diverge with decreasing temperature (ΔV_{cell} = 20 Å^3 at 250 K, ΔV_{cell} = 30 Å^3 at 225 K), until 210 K where HS_{II} phase becomes unstable (ΔV_{cell} = 40 Å^3).

It will kept in mind that all discrepancies appearing in this section arise partly from assuming one force field for I and II, in particular for long range van der Waals interactions. Nevertheless, the observed trends should not be changed.

6. Conclusions

Starting from the potential energy surface of the [Fe(PM BIA)$_2$(NCS)$_2$] complex obtained by DFT calculations on its distorted molecular geometry, Morse two body Fe N interactions have been evaluated for both spin states of the orthorhombic polymorph (*I*). The potential wells and the equilibrium distances depend both of the nature of the bound *N* atom and of the spin state of the Fe^{2+} ion. An adjustment of other two body potentials, combined with van der Waals interactions, allow then to calculate vibration modes (I.R. and Raman) of the molecule in its two spin states by molecular simulation. In agreement with the experimental molecular geometry, the FeN_6 octahedron is found more distorted in the high spin state than in the low spin one, as exhibited by distance (Δd_{HS} = 0.21 > Δd_{LS} = 0.03 Å) and angle extrema ($\Delta\theta_{HS}$ = 26.4 > $\Delta\theta_{LS}$ = 13.7 deg). Transferring the two obtained fields to the crystal state, molecular simulations give structural informations on the crystal lattice of the orthorhombic phases. Intermolecular interactions show evidence of hydrogen bonding between *NCS* sulfur end atoms with nearest neighbors hydrogen belonging to the aromatic cycles. The evolution of the structure with temperature shows that the $LS \rightarrow HS$ transition occurs at $T_{1/2}\uparrow$ = 120 K which is 50 K lower than the experimental value. The corresponding volume change of the unit cell, ΔV_{cell} = 121 Å^3, may be compared to the crystallographic data at 170 K (ΔV_{cell} = 57.4 Å^3).

The change of the transition enthalpy, $\Delta^{MD}H_{1/2}$ = 14 ± 2 kJ/mol corresponds to the transition temperature $T_{1/2}$ = 150 K. If $T_{1/2}$ agrees with experiments ($T_{1/2}\uparrow$ = 173 K and $T_{1/2}\downarrow$ = 168 K), the *MD* enthalpy value lies a little above experimental measurements ($\Delta^{DSC}H_{LS\rightarrow HS}$ = 10.06 kJ/mol and 11.5 kJ/mol). A more precise determination of $\Delta^{MD}H_{1/2}$ would certainly be obtained through the evaluation of the Gibbs free energy variation $\Delta^{MD}G_{LS\rightarrow HS}$ resulting from the integration of the hybrid classical Hamiltonian which contains potential and kinetic terms and which describes both *LS* and *HS* spin states.

The relative disagreement for $\Delta^{MD}H_{1/2}$ and for the structural results can also be accounted for by the drawbacks of a purely classical model in view of the prevailing quantum effects accounting below 100 K.

The molecular simulations have led to assess and complete the experimental (P,T) phase diagram of [Fe(PM BIA)$_2$(NCS)$_2$]. This is relevant to showing the domains of existence of the monoclinic polymorph (*II*) generated by its two spin states. Furthermore the delimitation of the different domains allowed generating two triple points:

- for LS_I, HS_I and HS_{II} equilibrium: at 170 K and ~3.0 kbar,
- for LS_I, LS_{II} and HS_{II} equilibrium, at 100 K and ~6.8 kbar.

On the other hand, the lack of data at low temperature leads us to provide neutron diffraction experiments on the LS_1 phase, in or der to precise the (P,T) phase diagram below 175 K, in particular the stability range of this phase. These experiments are underway.

Indirectly, this work contributes to the general efforts done to identify the factors allowing to control the existence of the *SCO* phenomenon in molecular materials. This demonstrates how the packing may affect the geometry of a ligand and then the *SCO* prop erties. All the present results would be improved by using specific force field derived for each one of the four phases. This implies obtaining new van der Waals force field parameters as a function of the spin state and of the symmetry.

References

[1] J.F. Létard, S. Montant, P. Guionneau, P. Martin, A. Le Calvez, E. Freysz, D. Chasseau, R. Lapouyade, O. Kahn, J. Chem. Soc. Chem. Comm. (1997) 745;
J. Degert, N. Lascoux, S. Montant, S. Létard, E. Freysz, G. Chastenet, J.-F. Létard, Chem. Phys. Lett. Lett. 415 (2005) 206.
[2] J.F. Létard, P. Guionneau, L. Rabardel, J.A.K. Howard, A.E. Goeta, D. Chasseau, O. Kahn, Inorg. Chem. 37 (1998) 4432.
[3] H. Daubric, J. Kliava, P. Guionneau, D. Chasseau, J.F. Létard, O. Kahn, J. Phys. Condens. Matter 12 (2000) 5481.
[4] M. Marchivie, P. Guionneau, J.F. Létard, D. Chasseau, Acta Cryst. B 59 (2003) 479.
[5] J.-F. Létard, G. Chastanet, O. Nguyen, S. Marcen, M. Marchivie, P. Guionneau, D. Chasseau, P. Gütlich, Monatsh. Chem. 134 (2003) 165.
[6] J. Ichiyanagi, L. Hébert, H. Toupet, E. Cailleau, P. Collet, J.-F. Guionneau, Solid State Phenom. 112 (2006) 81.
[7] M. Buron-Le Cointe, J. Hébert, C. Baldé, N. Moisan, L. Toupet, P. Guionneau, J.F. Létard, E. Freysz, H. Cailleau, E. Collet, Phys. Rev. B 85 (2012) 064114.
[8] A. Rotaru, F. Varret, E. Codjovi, K. Boukheddaden, J. Linares, A. Stancu, P. Guionneau, J.-F. Létard, J. Appl. Phys. 106 (2009) 053515.
[9] M. Marchivie, P. Guionneau, J.F. Létard, D. Chasseau, Acta Cryst. B 61 (2005) 25.
[10] J.-F. Létard, J. Mater. Chem. 16 (2006) 2550.
[11] P.A. Szilagyi, S. Dorbes, G. Molnar, J.A. Real, Z. Homonnay, C. Faulmann, A. Bousseksou, J. Phys. Chem. Solids 69 (2008) 2681.
[12] H.J. Shepherd, P. Rosa, L. Vendier, N. Casati, J.F. Létard, A. Bousseksou, P. Guionneau, G. Molnr, Phys. Chem. Chem. Phys. 14 (2012) 5265.
[13] V. Ksenofontov, G. Levchenko, H. Spiering, P. Gütlich, J.F. Létard, Y. Bouhedja, O. Kahn, Chem. Phys. Lett. 294 (1998) 545.
[14] P. Hohenberg, W. Kohn, Phys. Rev. B 136 (1964) 864.
[15] W. Kohn, L.J. Sham, Phys. Rev. A 140 (1965) 1133.
[16] L. Kabalan, S.F. Matar, Chem. Phys. 359 (2009) 14;
S.F. Matar, J.F. Létard, Z. Naturf. B 65b (2010) 565.
[17] Y. Zhu, Y. Su, X. Li, Y. Wang, G. Chen, Chem. Phys. Lett. 455 (2008) 354.
[18] GAUSSIAN 03, Revision C.02, M.J. Frisch, G.W. Trucks, H.B. Schlegel, G.E. Scuseria, M.A. Robb, J.R. Cheeseman, J.A. Montgomery Jr, T. Vreven, K.N. Kudin, J.C. Burant, J.M. Millam, S.S. Iyengar, J. Tomasi, V. Barone, B. Mennucci, M. Cossi, G. Scalmani, N. Rega, G.A. Petersson, H. Nakatsuji, M. Hada, M. Ehara, K. Toyota, R. Fukuda, J. Hasegawa, M. Ishida, T. Nakajima, Y. Honda, O. Kitao, H. Nakai, M. Klene, X. Li, J.E. Knox, H.P. Hratchian, J.B. Cross, V. Bakken, C. Adamo, J. Jaramillo, R. Gomperts, R.E. Stratmann, O. Yazyev, A.J. Austin, R. Cammi, C. Pomelli, J.W. Ochterski, P.Y. Ayala, K. Morokuma, G.A. Voth, P. Salvador, J.J.D. Dannenberg, V.G. Zakrzewski, S. Dapprich, A.D. Daniels, M.C. Strain, O. Farkas, D.K. Malick, A.D. Rabuck, K. Raghavachari, J.B. Foresman, J.V. Ortiz, Q. Cui, A.G. Baboul, S. Clifford, J. Cioslowski, B.B. Stefanov, G. Liu, A. Liashenko, P. Piskorz, I. Komaromi, R.L. Martin, D.J. Fox, T. Keith, M.A. Al-Laham, C.Y. Peng, A. Nanayakkara, M. Challacombe, P.M.W. Gill, B. Johnson, W. Chen, M.W. Wong, C. Gonzalez, J.A. Pople, Gaussian, Inc., Wallingford CT, 2004.
[19] M. Reiher, Inorg. Chem. 41 (2002) 6928.
[20] DL_POLY 2.20, W. Smith, T.R. Forester, I.T. Todorov, SFTC Daresbury Laboratory, Warrington, UK, 2009.
[21] P. Guionneau, C. Brigouleix, Y. Barrans, A.E. Goeta, J.F. Létard, J.A.K. Howard, J. Gaultier, D. Chasseau, C.R. Acad, Sci. Ser. IIc 4 (2001) 161.
[22] C.P. Slichter, H.G. Drickamer, J. Chem. Phys. 56 (1972) 2142.
[23] C. Cantin, J. Kliava, A. Marbeuf, D. Mikaïlitchenko, Eur. Phys. J. B 12 (1999) 525.
[24] V. Legrand, F. Le Gac, P. Guionneau, J.F. Létard, J. Appl. Cryst. 41 (2008) 637.
[25] A. Takada, C.R.A. Catlow, G.D. Price, J. Phys. Condens. Matter. 7 (1995) 8659.
[26] H. Sun, J. Phys. Chem. B 102 (1998) 7338;
S.W. Bunte, H. Sun, J. Phys. Chem. B 104 (2000) 2477;
J. Yang, Y. Ren, A. Tian, H. Sun, J. Phys. Chem. B 104 (2000) 4951;
M.J. McQuaid, H. Sun, D. Rigby, J. Comput. Chem. 25 (2004) 61.
[27] P. Cazade, Thèse, Université de Pau et des Pays de l'Adour, 2008.
[28] H.J.C. Berendsen, J.P.M. Postma, W. van Gunsteren, A. DiNola, J.R.J. Haak, J. Chem. Phys. 81 (1984) 3684.
[29] M.P. Allen, D.J. Tildesley, Computer Simulation of Liquids, Clarendon Press, Oxford, 1989.
[30] A. Hoeffer, Thesis, Mainz Universität, 2000.
[31] D. Mondieig, P. Négrier, P. Guionneau, Internal Report, Université de Bordeaux, 2008.
[32] P. Guionneau, M. Marchivie, G. Bravic, J.F. Létard, D. Chasseau, J. Mater. Chem. 12 (2002) 2546.